Enhancement of Magneto-Chiral Dichroism Intensity by Chemical Design: The Key Role of Magnetic-Dipole Allowed Transitions

Chong-Yang Li, Langit Cahya Adi, Kevin Paillot, Ivan Breslavetz, La-Sheng Long, Lan-Sun Zheng, Geert Rikken, Cyrille Train, Xiang-Jian Kong, Matteo Atzori

Enhancement of Magneto-Chiral Dichroism Intensity by Chemical Design: The Key Role of Magnetic-Dipole Allowed Transitions

[||]Chong Yang Li,[†] [||]Langit Cahya Adi,[‡] Kevin Paillot,[‡] Ivan Breslavetz,[‡] La-Sheng Long,[†] Lan-Sun Zheng,[†] Geert L. J. A. Rikken,[‡] Cyrille Train,[‡] Xiang-Jian Kong*[†] and Matteo Atzori*[‡]

† Collaborative Innovation Center of Chemistry for Energy Materials, State Key Laboratory of Physical Chemistry of Solid Surfaces and Department of Chemistry, College of Chemistry and Chemical Engineering, Xiamen University, Xiamen, China.

‡ Laboratoire National des Champs Magnétiques Intenses (LNCMI), Univ. Grenoble Alpes, INSA Toulouse, Univ. Toulouse Paul Sabatier, EMFL, CNRS, Grenoble, France.

Supporting Information Placeholder

ABSTRACT: Here we report on the strong Magneto-Chiral Dichroism (MChD) detected through Visible and Near Infrared light absorption up to 5.0 T on $\{Er_5Ni_6\}$ metal clusters obtained by reaction of enantiopure chiral ligands and Ni^{II} and Er^{III} precursors. Single-crystal diffraction analysis reveals that these compounds are *3d-4f* heterometallic clusters showing helical chirality. MChD spectroscopy reveals a high g_{MChD} dissymmetry factor of ca. 0.24 T^{-1} (T = 4.0 K, $\boldsymbol{B}$ = 1.0 T) for the $^4I_{13/2}\leftarrow{}^4I_{15/2}$ magnetic-dipole allowed electronic transition of the Er^{III} centers. This record value is one/two order of magnitude higher than that of the *d-d* electronic transitions of the Ni^{II} ions and the others *f-f* electric-dipole induced transitions of the Er^{III} centers. These findings clearly show the key role that magnetic-dipole allowed transitions have in the rational design of chiral lanthanide systems showing strong MChD.

Functional materials responsive to chirality, light and magnetism are attracting great attention for their potential in many technological applications such as light-emitting displays, chiral sensors, magnetic data storage and optical readout.[1–3] Among the chiro-optical properties exhibited by molecular materials, Magneto-Chiral Dichroism (MChD), the differential absorption or emission of unpolarized light that chiral systems exhibit when a magnetic field is applied parallel to a light wavevector,[4–7] is particularly interesting for its unprecedented potential as an alternative approach to the Faraday effect[8,9] for the optical readout of magnetic data.[3,10,11] Specifically, this consists in discriminating two orientations of the magnetization of a chiral magnetic material by measuring the differential absorption or emission of light without requiring light polarization.

To make this physical phenomenon a technological reality, the MChD response of chiral magnetic materials has to be maximized. In other words, to achieve a high degree of detectability, the differential absorption or emission of light in the presence of a magnetic field with respect to zero field absorption or emission should be as big as possible. This is quantified by the g_{MChD} dissymmetry factor, analogously to what is done in others chiroptical spectroscopies.[12]

To attain this purpose, chiral magnetic molecular systems are ideal systems for at least two reasons. First, chiral structural features can be easily introduced by molecular methods. Different chiral features (central, axial, planar, or helical chirality) can be introduced by changing the nature of the ligands and/or the assembly schemes.[13,14] Second, electronic transitions of different nature can be addressed, spanning from n-π^* and π-π^* transitions of purely organic systems, to *d-d* and *f-f* electronic transitions of transition metal and lanthanide centers, respectively.

Owing to their intrinsic strong spin-orbit coupling, recent studies have been focused on the MChD of lanthanide complexes[15–21] and heterometallic *3d-4f* chiral clusters.[22] These latter, featuring Dy^{III} and Ni^{II} ions in a $\{Dy_5Ni_6\}$ core, have shown MChD for the electronic transitions of both metal ions, but with limited g_{MChD} factors.[22] Accordingly, here we have applied chemical substitution principles for lanthanide-containing systems to go from $\{Dy_5Ni_6\}$ to $\{Er_5Ni_6\}$ to unambiguously determine the role of magnetic-dipole allowed transitions on MChD intensity and tentatively increase the MChD response. Indeed, while Dy^{III} does not have any magnetic-dipole allowed electronic transitions in the UV-Vis-NIR range,[23–25] Er^{III} features a $^4I_{13/2}\leftarrow{}^4I_{15/2}$ magnetic-dipole allowed electronic transition at ca. 1500 nm as well as a multitude of electric-dipole induced transitions in the visible range.[24–26] This chemical modification is expected to increase the g_{MChD} dissymmetry factor for the magnetic-dipole allowed transition, while the other transitions and those of the Ni^{II} are expected to be of the same order of magnitude.[22]

We have therefore prepared enantiopure $\{Er_5Ni_6\}$ complexes formulated as $[Er_5Ni_6(R/S\text{-HL})_6(AcO)_3(\mu_3\text{-}OH)_9(H_2O)_6](ClO_4)_3{\cdot}15H_2O$ (**1-(*R*/*S*)**), H_3L = *(R/S)*-(2-hydroxy-3-methoxy benzyl)-serine)) by reaction of enantiopure chiral multidentate ligands *(S)*-H_3L and *(R)*-H_3L, with $Er(ClO_4)_3$

and $Ni(AcO)_2$ (AcO^- = acetate) under reflux conditions and controlled pH. Their optical activity was checked by Circular Dichroism spectroscopy (Figure S1). High-resolution electrospray ionization mass spectrometry revealed several clear isotope peaks framing main signals at m/z = 3151.66, 1526.37, and 997.92 m/z for both **1-*(S)*** and **1-*(R)***. Following the crystal structure determination presented thereafter, they correspond to the $[Er_5Ni_6(OH)_9(X\text{-}HL)_6(AcO)_3(ClO_4)_2]$ (X = *S*, *R*) species (Figure S2). All peaks are consistent with the theoretical distributions (Figure S2 and experimental section), and almost all show an intact metal-core frame of the cluster, indicating a high stability of the self-assembled $\{Er_5Ni_6\}$ cluster, similarly to what observed for the $\{Dy_5Ni_6\}$ analogues.[22]

1-*(S)* and **1-*(R)*** crystallize as rhombohedral crystals in the orthorhombic $P2_12_12_1$ space group (Table S1) and are isostructural to the $\{Dy_5Ni_6\}$ analogues. Owing to their isostructurality, here we recall only the most salient features of the crystal and molecular structure, while a detailed description can be found elsewhere.[22] They feature one crystallographically independent cationic cluster core formulated as $[Er_5Ni_6(X\text{-}HL)_6(Ac)_3(\mu_3OH)_9(H_2O)_6]^{3+}$ (X = *S*, *R*), three perchlorate counterions, and fifteen water molecules of crystallization (Figure 1).

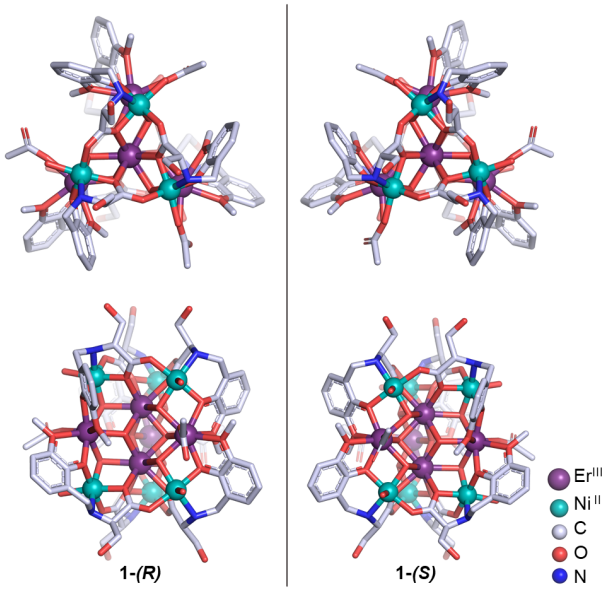

Figure 1. Molecular structures of **1-*(R)*** and **1-*(S)*** with helical arrangement of the ligands around the coordinated metals highlighted. See legend for color codes. Counterions, crystallization water molecules and H atoms are omitted for graphical clarity.

The cationic cluster core is constituted by five Er^{III} and six Ni^{II} ions bridged by nine hydroxide ions, six HL^{2-} bridging ligands and three acetate ions. The five Er^{III} ions are linked together by three μ_3-OH^- bonds to form a $[Er_5(\mu_3\text{-}OH)_3]^{12+}$ core featuring a compressed trigonal bipyramid. The two Er^{III} ions occupying the axial positions are nona-coordinated while the three Er^{III} ions occupying the equatorial positions are octa-coordinated. The five Ni^{II} ions are hexacoordinated and occupy peripheral positions in the molecular structure. Overall, the chiral ligands drive the chiral features of the molecular structure and asymmetrically distorts the coordination geometry of Ni^{II} and Er^{III} ions.

Magnetic susceptibility measurements were performed on both microcrystalline powder (**1-*(S)***) and an oriented single crystal (**1-*(R)***) with the magnetic field ***B*** oriented parallel to the *c* crystallographic axis (Figures S3 and S4). The room temperature molar magnetic susceptibility times the temperature, $\chi_M T$, assumes values of 64.07 and 63.49 $cm^3\ K\ mol^{-1}$ for **1-*(S)*** and **1-*(R)***, respectively, and are consistent with the expected value (64.66 $cm^3\ K\ mol^{-1}$) for six Ni^{II} (S = 1, g = 2.2) and five Er^{III} (J = 15/2, g = 6/5) uncorrelated ions. As the temperature is decreased from 300 to 150 K, the $\chi_M T$ values only slightly decrease, while upon further lowering of the temperature they decrease down to 35.34 and 34.37 $cm^3\ mol^{-1}$ K at 2.0 K, respectively. This behavior might arise from the Zero Field Splitting and Stark effects in Ni^{II} and Er^{III} and/or antiferromagnetic interactions between them. The complexity of the system precludes the possibility to finely quantify these conflicting phenomena. The magnetic behavior observed for the microcrystalline powder and the oriented crystal is similar, denoting a low degree of magnetic anisotropy for the Er^{III} ions.[27] This is not surprising on the basis of their coordination geometries. At T = 2.0 K, the magnetization saturates at ca. 37 μ_B for both the microcrystalline powder and the oriented single crystal, in agreement with typical values observed for six Ni^{II} ($M_S = 6 \times 2.2\ \mu_B$) and five Er^{III} ions ($M_S = 5 \times 4.7\ \mu_B$) centers without strong magnetic anisotropy.[28]

Absorption spectra were recorded on single crystals of **1-*(R)*** and **1-*(S)*** with Vis-NIR unpolarized light propagating along the *c* axis. The thermal variation (4.0-290 K) of the wide-range (400-1600 nm) absorption spectrum for **1-*(R)*** is presented in Figure 2.

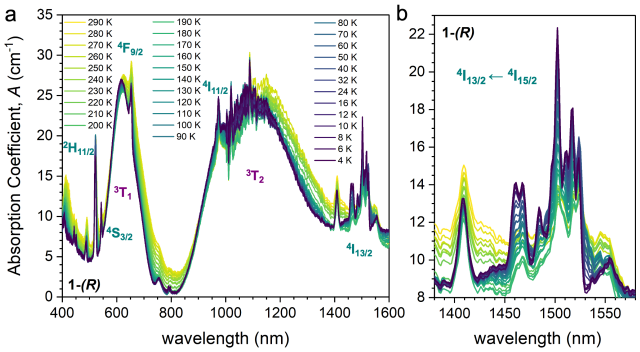

Figure 2. Thermal variation of the absorption coefficient for a single crystal of **1-*(R)*** (***k***||*c*) in the wide 400-1600 nm range (a) and a zoom of the 1380-1580 nm range (b). The terms of the main transitions are highlighted in green and purple for Er^{III} and Ni^{II}, respectively (only excited states terms are shown in panel a).

The investigated range shows multiple absorption peaks. The broad absorption bands are associated with the *d-d* electronic transitions involving the $^3A_2$ ground state and the ^3T_n (n = 1, 2) spectroscopic terms of the Ni^{II} ions,[22,29] while the sharp bands are associated with the *f-f* transitions involving the $^4I_{15/2}$ ground state and the spectroscopic levels deriving from the ^4I, ^4F, ^4S and ^2H spectroscopic terms of the Er^{III} centers (Figure 2, Table 1).[24–26]

Table 1. Assignment of the Ni^{II} and Er^{III} absorption peaks and g_{MChD} values at T = 4.0 K and B = 1.0 T

λ (nm)	Electronic transition	g_{MChD} (T^{-1}) (B = 1.0 T), λ (nm)
487	$^4F_{7/2} \leftarrow {}^4I_{15/2}$	0.009(2), 485.1
520	$^2H_{11/2} \leftarrow {}^4I_{15/2}$	0.004(2), 519.0
543	$^4S_{3/2} \leftarrow {}^4I_{15/2}$	0.008(2), 544.3
617	$^3T_2 \leftarrow {}^3A_2$	0.005(2), 615.6
653	$^4F_{9/2} \leftarrow {}^4I_{15/2}$	0.02(1), 653.1
973	$^4I_{11/2} \leftarrow {}^4I_{15/2}$	0.03(1), 973.4
1180	$^3T_1 \leftarrow {}^3A_2$	0.01(1), 1180.8
1400-1560	$^4I_{13/2} \leftarrow {}^4I_{15/2}$	0.24(1), 1516.2

MChD measurements were performed at T = 4.0 K with an alternating magnetic field $\boldsymbol{B}$ applied along $\boldsymbol{k}$ within the 0.0–2.0 T range. Figure 3 shows the $\boldsymbol{B}$ dependence of the MChD spectra for **1-*(R)*** along the *c* crystallographic axis.

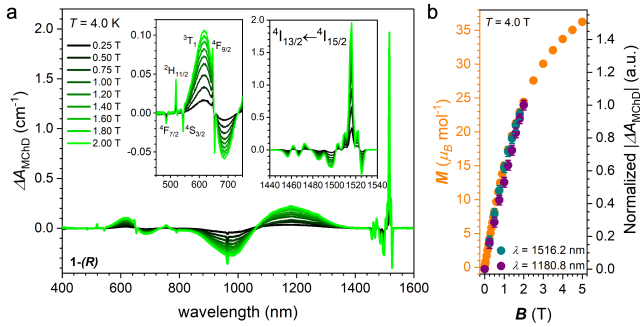

Figure 3. (a) Magnetic field dependence of ΔA_{MChD} for **1-*(R)*** at T = 4.0 K. Insets show the details of the most intense MChD signals. (b) Magnetic field dependence of ΔA_{MChD} (λ = 1516.2, 1180.8 nm) compared to magnetization data recorded on an oriented single crystal ($\boldsymbol{B}||c$).

MChD signals are observed for each electronic transition detected in absorption. The most intense contributions are associated to the $^4I_{13/2} \leftarrow {}^4I_{15/2}$ magnetic-dipole allowed transition for Er^{III} and the $^3T_1 \leftarrow {}^3A_2$ transition for Ni^{II}. At 4.0 K, as the magnetic field magnitude increases, the MChD intensity increases following the overall magnetization of the system.[10,30,31] This is shown in Figure 3b for the most intense contributions of Er^{III} and Ni^{II} centers compared to magnetization data recorded on an oriented single-crystal. It can also be noted that higher ΔA_{MChD} values can be obtained if $\boldsymbol{B}$ is increased further as $\boldsymbol{M}$ does not reach saturation at 2.0 T. We have thus extended for the first time our MChD investigations to magnetic fields up to ±5.0 T taking advantage of the resistive magnets of the LNCMI-CNRS French high magnetic field facility. As expected, between 2.0 and 5.0 T, ΔA_{MChD} increases further, in agreement with magnetic measurements, and, for the $^4I_{13/2} \leftarrow {}^4I_{15/2}$ transition, reaches the remarkable value of ΔA_{MChD} = 2.79(1) cm^{-1} at 5 T (Figure S5).

The analysis of the MChD and absorption spectra (T = 4.0 K, B = 1.0 T), allow to estimate the g_{MChD} factors (see SI) for the observed transitions (Table 1). It can be clearly seen that the $^4I_{13/2} \leftarrow {}^4I_{15/2}$ magnetic-dipole transition (ΔJ = 0, ±1), with a high ΔA_{MChD} response at λ = 1516.2 nm and a relative low absorption coefficient provides a g_{MChD} of 0.24 T^{-1}. This high value is of the same order of magnitude of that observed for the $^2F_{5/2} \leftarrow {}^2F_{7/2}$ magnetic-dipole allowed transition of Yb^{III} in a helicenic complex[20] and is one or two orders of magnitude higher that that observed for the others *d-d* or *f-f* transitions in {Er_5Ni_6} (Table 1), and in {Dy_5Ni_6}.[22] It is useful to recall here that *ab initio* theoretical calculations have shown that the electric quadrupole contribution to the MChD of Ni^{II} *d-d* transitions is two orders of magnitude smaller than that originating from electric dipole transition moments.[29] A similar contribution is expected for electric-dipole induced or magnetic dipole allowed *f-f* transitions.

Temperature dependence studies show MChD signals with similar intensities and opposite signs for the two enantiomers (Figure S6). The thermal variation (4.0-290 K) of the wide range (400-1600 nm) MChD spectrum for **1-*(R)*** is reported in Figure 4 while that of **1-*(S)*** is shown in Figure S7.

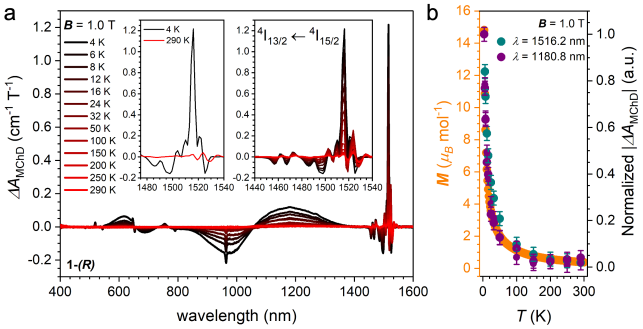

Figure 4. Temperature dependence of ΔA_{MChD} for **1-*(R)*** at B = 1.0 T. Insets show the details of the most intense MChD signals. (b) Temperature dependence of ΔA_{MChD} (λ = 1516.2, 1180.8 nm) compared to magnetization data.

As the temperature increases, the intensity of the MChD signals decreases, following the temperature dependence of the magnetization regardless the nature of the electronic transition and the nature of the chromophore (Figure 4b). This is in agreement with previous studies on the {Dy_5Ni_6} analogue.[22] At room temperature, the most intense MChD signal is still detectable while the others are below the detection limits of our setup. Inset of Figure 4 shows the difference in MChD signal shape between the low temperature regime, where the MChD shows mostly absorption lineshapes, indicating that a *C* term MChD is dominating, and the high temperature regime, where the derivative-type lineshape indicates the dominance of a *T*-independent MChD *A* term.[15] At 290 K, the g_{MChD} (λ = 1530 nm) is 0.054(1) T^{-1}, which is the strongest g_{MChD} value ever reported at room temperature.

In conclusion, we have investigated the MChD properties of a *3d-4f* heterometallic chiral cluster made of Er^{III} and Ni^{II} ions. By exploiting the chemical substitution principles of lanthanide ions, we have introduced Er^{III}, whose MChD properties were never investigated so far, in a previously known MChD-active chiral cluster. This has been done to prove the role of the electronic transitions on MChD intensity as Er^{III} shows multiple transitions having different nature. Indeed, the $^4I_{13/2} \leftarrow {}^4I_{15/2}$ magnetic-dipole allowed transition has shown the most intense ΔA_{MChD} response and the most intense g_{MChD} dissymmetry factor with respect to the other observed transitions and those of the isostructural {Dy_5Ni_6} analogue,[22] being detectable up to room temperature.

These results unambiguously demonstrate the key role that the electronic transitions nature has in the MChD of lanthanide systems. In particular, the magnetic-dipole allowed character should be considered of foremost importance in the chemical design of functional chiral materials showing strong MChD. The strong MChD response observed here even in the absence of high magnetic anisotropy features opens great perspectives. Indeed, the rational design of

highly anisotropic Er^{III} chiral complexes is expected to lead to even stronger MChD responses that can coexist with relevant single-molecule magnets properties[27,28] or circular polarized emission.[32,33]

ASSOCIATED CONTENT

Supporting Information

Additional figures, crystallographic tables, experimental details, materials and methods.

AUTHOR INFORMATION

[||] C.Y.L and L.C.A contributed equally to this paper.

Corresponding Authors

matteo.atzori@lncmi.cnrs.fr, xjkong@xmu.edu.cn

Notes

The authors declare no competing financial interests.

ACKNOWLEDGMENT

The French National Research Agency (ANR) is acknowledged for financial support through MaChiNaCo (ANR-19-CE09-0018), Switch-MChD (ANR-23-CE07-0003) and PRINCIPE (ANR-23-CE07-0015) projects. This project has received financial support from the CNRS through the MITI interdisciplinary programs through its exploratory research program. We acknowledge the support of the LNCMI-CNRS, member of the European Magnetic Field Laboratory (EMFL). We gratefully acknowledge the financial support from the National Natural Science Foundation of China (Grant Nos. 92161104, 92161203 and 92361301).

REFERENCES

(1) Yang, S.-H.; Naaman, R.; Paltiel, Y.; Parkin, S. S. P. Chiral Spintronics. *Nat. Rev. Phys.* **2021**, *3*, 328–343.
(2) Kuang, H.; Xu, C.; Tang, Z. Emerging Chiral Materials. *Adv. Mater.* **2020**, *32*, 2005110.
(3) Galán-Mascarós, J. R. Bring to Light. *Nat. Phys.* **2015**, *11*, 7–8.
(4) Atzori, M.; Rikken, G. L. J. A.; Train, C. Magneto-Chiral Dichroism: A Playground for Molecular Chemists. *Chem. Eur. J.* **2020**, *26*, 9784–9791.
(5) Atzori, M.; Train, C.; Hillard, E. A.; Avarvari, N.; Rikken, G. L. J. A. Magneto-chiral Anisotropy: From Fundamentals to Perspectives. *Chirality* **2021**, *33*, 844–857.
(6) Rikken, G. L. J. A.; Raupach, E. Observation of Magneto-Chiral Dichroism. *Nature* **1997**, *390*, 493–494.
(7) Barron, L. D.; Vrbancich, J. Magneto-Chiral Birefringence and Dichroism. *Mol. Phys.* **1984**, *51*, 715–730.
(8) Serber, R. The Theory of the Faraday Effect in Molecules. *Phys. Rev.* **1932**, *41*, 489–506.
(9) Faraday, M. I. Experimental Researches in Electricity.—Nineteenth Series. *Philos. Trans. R. Soc. Lond.* **1846**, *136*, 1–20.
(10) Train, C.; Gheorghe, R.; Krstic, V.; Chamoreau, L.-M.; Ovanesyan, N. S.; Rikken, G. L. J. A.; Gruselle, M.; Verdaguer, M. Strong Magneto-Chiral Dichroism in Enantiopure Chiral Ferromagnets. *Nat. Mater.* **2008**, *7*, 729–734.
(11) Barron, L. D. Chirality and Magnetism Shake Hands. *Nat. Mater.* **2008**, *7*, 691–692.
(12) *Comprehensive Chiroptical Spectroscopy*; Berova, N., Polavarapu, P. L., Nakanishi, K., Woody, R. W., Eds.; John Wiley & Sons, Inc.: Hoboken, NJ, USA, 2011.
(13) L. D. Barron, *Molecular Light Scattering and Optical Activity*, Cambridge University Press, second edition, 2004.
(14) Train, C.; Gruselle, M.; Verdaguer, M. The Fruitful Introduction of Chirality and Control of Absolute Configurations in Molecular Magnets. *Chem. Soc. Rev.* **2011**, *40*, 3297.
(15) Atzori, M.; Dhbaibi, K.; Douib, H.; Grasser, M.; Dorcet, V.; Breslavetz, I.; Paillot, K.; Cador, O.; Rikken, G. L. J. A.; Le Guennic, B.; Crassous, J.; Pointillart, F.; Train, C. Helicene-Based Ligands Enable Strong Magneto-Chiral Dichroism in a Chiral Ytterbium Complex. *J. Am. Chem. Soc.* **2021**, *143*, 2671–2675.
(16) Raju, M. S.; Dhbaibi, K.; Grasser, M.; Dorcet, V.; Breslavetz, I.; Paillot, K.; Vanthuyne, N.; Cador, O.; Rikken, G. L. J. A.; Le Guennic, B.; Crassous, J.; Pointillart, F.; Train, C.; Atzori, M. Magneto-Chiral Dichroism in a One-Dimensional Assembly of Helical Dysprosium(III) Single-Molecule Magnets. *Inorg. Chem.* **2023**, *62*, 17583–17587.
(17) Ceolín, M.; Goberna-Ferrón, S.; Galán-Mascarós, J. R. Strong Hard X-Ray Magnetochiral Dichroism in Paramagnetic Enantiopure Molecules. *Adv. Mater.* **2012**, *24*, 3120–3123.
(18) Mitcov, D.; Platunov, M.; Buch, C. D.; Reinholdt, A.; Døssing, A. R.; Wilhelm, F.; Rogalev, A.; Piligkos, S. Hard X-Ray Magnetochiral Dichroism in a Paramagnetic Molecular 4f Complex. *Chem. Sci.* **2020**, *11*, 8306–8311.
(19) Taniguchi, K.; Nishio, M.; Kishiue, S.; Huang, P.-J.; Kimura, S.; Miyasaka, H. Strong Magnetochiral Dichroism for Visible Light Emission in a Rationally Designed Paramagnetic Enantiopure Molecule. *Phys. Rev. Mater.* **2019**, *3*, 45202.
(20) Dhbaibi, K.; Grasser, M.; Douib, H.; Dorcet, V.; Cador, O.; Vanthuyne, N.; Riobé, F.; Maury, O.; Guy, S.; Bensalah-Ledoux, A.; Baguenard, B.; Rikken, G. L. J. A.; Train, C.; Le Guennic, B.; Atzori, M.; Pointillart, F.; Crassous, J. Multifunctional Helicene-Based Ytterbium Coordination Polymer Displaying Circularly Polarized Luminescence, Slow Magnetic Relaxation and Room Temperature Magneto-Chiral Dichroism. *Angew. Chem.* **2023**, *135*, No. e202215558.
(21) Pointillart, F.; Atzori, M.; Train, C. Magneto-Chiral Dichroism of Chiral Lanthanide Complexes. *Inorg. Chem. Front.* **2024**, *11*, 1313–1321.
(22) Wang, X.; Wang, S.-Q.; Chen, J.-N.; Jia, J.-H.; Wang, C.; Paillot, K.; Breslavetz, I.; Long, L.-S.; Zheng, L.; Rikken, G. L. J. A.; Train, C.; Kong, X.-J.; Atzori, M. Magnetic 3d–4f Chiral Clusters Showing Multimetal Site Magneto-Chiral Dichroism. *J. Am. Chem. Soc.* **2022**, *144*, 8837–8847.
(23) Kofod, N.; Arppe-Tabbara, R.; Sørensen, T. J. Electronic Energy Levels of Dysprosium(III) Ions in Solution. Assigning the Emitting State and the Intraconfigurational *4f–4f* Transitions in the Vis–NIR Region and Photophysical Characterization of Dy(III) in Water, Methanol, and Dimethyl Sulfoxide. *J. Phys. Chem. A* **2019**, *123*, 2734–2744.
(24) Richardson, F. S. Selection Rules for Lanthanide Optical Activity. *Inorg. Chem.* **1980**, *19*, 2806–2812.
(25) Bünzli, J.-C. G. Benefiting from the Unique Properties of Lanthanide Ions. *Acc. Chem. Res.* **2006**, *39*, 53–61.
(26) Amin, J.; Dussardier, B.; Schweizer, T.; Hempstead, M. Spectroscopic Analysis of Er^{3+} Transitions in Lithium Niobate. *J. Lumin.* **1996**, *69*, 17–26.
(27) Briganti, M.; Lucaccini, E.; Chelazzi, L.; Ciattini, S.; Sorace, L.; Sessoli, R.; Totti, F.; Perfetti, M. Magnetic Anisotropy Trends along a Full 4f-Series: The f^{n+7} Effect. *J. Am. Chem. Soc.* **2021**, *143*, 8108–8115.
(28) Sorace, L.; Benelli, C.; Gatteschi, D. Lanthanides in Molecular Magnetism: Old Tools in a New Field. *Chem. Soc. Rev.* **2011**, *40*, 3092.
(29) Atzori, M.; Ludowieg, H.; Cortijo, M.; Breslavetz, I.; Paillot, K.; Rosa, P.; Train, C.; Autschbach, J.; Hillard, E. A.; Rikken, G. L. J. A. Validation of Microscopic Magneto-Chiral Dichroism Theory. *Sci. Adv.* **2021**, *7*, eabg2859.
(30) Atzori, M.; Breslavetz, I.; Paillot, K.; Inoue, K.; Rikken, G. L. J. A.; Train, C. A Chiral Prussian Blue Analogue Pushes Magneto-Chiral Dichroism Limits. *J. Am. Chem. Soc.* **2019**, *141*, 20022–20025.

(31) Atzori, M.; Breslavetz, I.; Paillot, K.; Rikken, G. L. J. A.; Train, C. Role of Structural Dimensionality in the Magneto-Chiral Dichroism of Chiral Molecular Ferrimagnets. *J. Mater. Chem. C* **2022**, *10*, 13939–13945.
(32) Zinna, F.; Di Bari, L. Lanthanide Circularly Polarized Luminescence: Bases and Applications. *Chirality* **2015**, *27*, 1–13.
(33) Willis, O. G.; Zinna, F.; Di Bari, L. NIR-Circularly Polarized Luminescence from Chiral Complexes of Lanthanides and d-Metals. *Angew. Chem.* **2023**, *135*, N° 202302358.

TOC Graphic